

Observation of second-order topological insulators in sonic crystals

Xiujuan Zhang^{1#}, Hai-Xiao Wang^{2#}, Zhi-Kang Lin², Yuan Tian¹, Biye Xie¹, Ming-Hui Lu^{1,3,†},
Yan-Feng Chen^{1,3}, and Jian-Hua Jiang^{2,†}

¹*National Laboratory of Solid State Microstructures and Department of Materials Science and Engineering, Nanjing University, Nanjing 210093, China*

²*School of Physical Science and Technology, and Collaborative Innovation Center of Suzhou Nano Science and Technology, Soochow University, 1 Shizi Street, Suzhou 215006, China*

³*Collaborative Innovation Center of Advanced Microstructures, Nanjing University, Nanjing 210093, China*

†Correspondence and requests for materials should be addressed to joejhjiang@hotmail.com (JHJ) or luminghui@nju.edu.cn (MHL)

These authors contributed equally to this work.

Topological insulators with unique gapless edge states have revolutionized the understanding of electronic properties in solid materials [1-4]. These gapless edge states are dictated by the topological invariants associated with the quantization of generalized Berry's phases of the bulk energy bands through the bulk-edge correspondence, a paradigm that can also be extended to acoustic and photonic systems [5-20]. Recently, high-order topological insulators (HOTIs) are proposed and observed, where the bulk topological invariants result in gapped edge states and in-gap corner or hinge states, going beyond the conventional bulk-edge correspondence [21-29]. However, the existing studies on HOTIs are restricted to tight-binding models which cannot describe the energy bands of conventional sonic/photonic crystals that are due to multiple Bragg scatterings. Here, we report theoretical prediction and experimental observation of acoustic second-order topological insulators (SOTI) in two-dimensional (2D) sonic crystals (SCs) beyond the tight-binding picture. We observe gapped edge states and degenerate in-gap corner states

which manifest bulk-edge correspondence in a hierarchy of dimensions. Moreover, topological transitions in both the bulk and edge states can be realized by tuning the angle of the meta-atoms in each unit-cell, leading to various conversion between bulk, edge and corner states. The emergent properties of the acoustic SOTIs open up a new route for topological designs of robust localized acoustic modes as well as topological transfer of acoustic energy between 2D, 1D and 0D modes.

Since the discovery of the quantum Hall effect, tremendous attention has been paid to topological phases of matters, as they go beyond the conventional classification of phases of matters based on spontaneous symmetry breaking, namely the well-known Ginzburg-Landau-Wilson paradigm [1-4]. Materials of the same symmetry can have distinct physical properties as characterized by the topological invariants of the energy bands below the band gap where the Fermi level resides. These topological invariants of an insulator result in robust gapless edge states and quantized physical responses (e.g., Hall conductance) [1-4]. Recently, by gapping out the edge states of topological insulators via various mechanisms, high-order topological insulators are created, where robust corner or hinge states emerge in the edge gap due to topological mechanisms [21-29].

It has been shown that the concept of topological insulators can be extended to acoustic waves in 2D SCs, leading to the discovery of 1D gapless edge states as waveguide channels robust against disorders [16-20]. The quest for high-order topological insulators in SCs, however, is not straightforward, since the existing proposals for HOTIs are based on tight-binding models with designed hopping configurations which cannot be realized in conventional SCs. In contrast, acoustic band structures in conventional SCs are associated with multiple Bragg scatterings,

which is not able to be described by tight-binding theory since the Wannier functions are not exponentially localized [30].

In this Letter, we construct acoustic SOTIs through topological crystalline insulators induced by gapping out a Dirac point at the Brillouin zone corner (i.e., the M point) of a 2D square-lattice SC. Topological edge states emerge at the boundary between two SCs with opposite Dirac masses. Since the band-degeneracy at the Dirac point is protected by the crystalline symmetries which are absent at the boundaries, the edge states have gapped spectrum, leading to 1D massive Dirac dispersions [14]. Remarkably, the Dirac masses of the 1D edge bands have opposite signs for the boundaries along the x and y directions, resulting in four Jackiw-Rebbi soliton states [31] localized at the corners shared by these boundaries (see Fig.1a).

To realize the above scenario, we design a 2D square-lattice SC with four meta-atoms in each unit-cell (Fig.1b). Each meta-atom is a polymethyl methacrylate block which can be regarded as impenetrable for acoustic waves. The choice of four meta-atoms as a unit-cell is in fact a doubling of the primitive cell but a minimal unit-cell that is consistent with the supercells for the edge and corner states [32]. By rotating the angle θ of the four meta-atoms, Dirac points can be created and gapped out in different ways. The topological phase diagram of the bulk acoustic band is illustrated in Fig. 1c, which contains two different phases: the normal band gap (NBG) phase and the SOTI phase. The latter corresponds to parity inversion as illustrated in Fig. 1c, where the M and Γ points have opposite parity for the two bands below the acoustic gap. The acoustic band structures for the NBG state with $\theta = -25^\circ$, the phase transition point at $\theta = 0$, and the SOTI state with $\theta = 45^\circ$, are given in Fig. 1d. The phase transition is signaled by an emergent four-fold degenerate Dirac point at the M point (see Supplemental Information for the details of the Dirac dispersion).

The double degeneracy on the Brillouin zone boundary lines MX and MY can be understood as a consequence of the glide symmetries, $G_x := (x, y) \rightarrow (\frac{a}{2} - y, \frac{a}{2} + x)$ and $G_y = (x, y) \rightarrow (\frac{a}{2} + y, \frac{a}{2} - x)$. When combined with the time-reversal operation T , the anti-unitary symmetry operators $\theta_j = G_j * T$ ($j = x, y$) enable double degeneracy at the Brillouin zone boundaries. For instance, $\theta_x^2 \psi_{n, \vec{k}} = e^{ik_x a} \psi_{n, \vec{k}}$ where $\psi_{n, \vec{k}}$ is a Bloch wavefunction for the acoustic pressure field with n and \vec{k} being the band index and wavevector, respectively. At the Brillouin zone boundary line MX, $\theta_x^2 = -1$, holds for all acoustic bands, inducing fermion-like double degeneracy. The four-fold degenerate Dirac point at the M point is due to the crossing between two pairs of doubly degenerate bands: the even-parity bands (the degenerate s and d wave states) and the odd parity bands (the degenerate p wave states) (see Fig. 1c). The gap opening for such a Dirac point gives rise to physics similar to the quantum spin Hall insulators [13,14,16]. In the Supplemental Information we establish the connection between the acoustic topological crystalline insulator and the Bernevig-Hughes-Zhang model [33] through a Hamiltonian theory. Indeed, the edge states carry finite orbital angular momentum (pseudo-spin) and exhibit pseudo-spin-wavevector locking as shown in Fig. 1e (see Supplemental Information for more details).

The two 1D edge bands of the topological crystalline insulator are supposed to cross each other at the $k_y = \frac{\pi}{a}$ ($k_x = \frac{\pi}{a}$) point for the boundaries along the y (x) axis, which is protected by the pseudo-time-reversal symmetries θ_y (θ_x). However, since the glide symmetry is broken on those boundaries, the edge bands are generally gapped, leading to massive 1D Dirac dispersions. The Dirac mass at the edges m_y (m_x) can be characterized by the frequency difference between the odd and even modes at the $k_y = \frac{\pi}{a}$ ($k_x = \frac{\pi}{a}$) point.

Remarkably, these Dirac masses are also tunable through the rotation angle of the meta-atoms. For instance, for the boundaries between the SC with $\theta = -25^\circ$ and the SC with $\theta = 45^\circ$, the gapped edge states along the x and y directions have Dirac masses of opposite signs. The sign difference of the Dirac mass on these edges leads to the formation of the Jackiw-Rebbi soliton modes on the corners shared by them. The emergence of these topological corner modes manifests bulk-edge correspondence in a hierarchy of dimensions: the bulk topology leads to the edge states, while the edge topology leads to the corner states, as shown in Fig. 1e. Such hierarchical bulk-edge correspondence is the smoking-gun signature of the HOTIs.

The physical properties of the helical edge states are studied for the SCs with $\theta = -45^\circ$ and $\theta = 45^\circ$ as an example. The choice of these two SCs is to minimize the band gap of the edge states. The edge dispersion is measured by the Fourier-transformed field scan method (see Methods) in experiments. The measured dispersion of the edge states agrees with the simulated results within the precision of the field scan method (see Fig. 2a). In addition, the distribution of the acoustic pressure field of the edge states measured in the experiments also agrees well with the simulation as shown in Fig. 2b. The phase profiles of the edge states at finite wavevectors show that the edge states carry phase vortices (see Fig. 2c), indicating finite orbital angular momentum (pseudo-spin). Moreover, the phase vortices have opposite winding directions for opposite wavevectors, in agreement with pseudo-spin-wavevector locking for the edge states of quantum spin Hall insulators. We corroborate these observations with a Hamiltonian analysis for the edge states and simulations on selective launching of the edge states via sources with finite orbital-angular-momentum in the Supplemental materials. These analysis confirm a massive Dirac equation description of the edge Hamiltonian as $H_j = v_j(k_j - \frac{\pi}{a})\sigma_z + m_j\sigma_x$ with $j = x, y$ for the edges along the x and y directions where $\sigma_z = \pm 1$ denotes pseudo-spin up and down,

respectively. The Dirac mass here equals to half of the frequency difference between the odd and even edge modes at $k_j = \frac{\pi}{a}$ with $j = x, y$.

Next we measure the corner states in a box-shaped geometry between the two SCs with $\theta = -25^\circ$ and $\theta = 45^\circ$. The frequencies of the eigenmodes are shown in Fig. 3a where four nearly degenerate corner modes with frequencies away from other modes are clearly visible. The sample in experiments for the box-shaped supercell geometry is shown in Fig. 3b. The simulated and measured distributions of the acoustic pressure field for one of the four corner states are shown in Figs. 3c and 3d, respectively. The experimental measurements agree well with the simulation, both indicating strongly localized acoustic modes. The agreement between the simulation and experiments confirms the observation of degenerate topological corner states in the edge gap.

We now study the topological phase transitions on the edge. We fix the angle of the meta-atoms of the NBG SC at the outside as $\theta_{out} = -25^\circ$, while tuning the angle of the meta-atoms for the SOTI SC lying inside the box-shaped supercell, θ_{in} . The band gaps of the edge states for boundaries along the x and y directions are controlled by the rotation angle θ_{in} . The edge phase diagram is shown in Fig. 4a where several transitions are manifested. The edge gap closing at $\theta_{in} = 0^\circ$ and $\theta_{in} = 90^\circ$ are caused by bulk band gap closing and bulk topological transitions. Remarkably, a transition at $\theta_{in} = 25^\circ$ appears where the edge gap closes at finite bulk band gap for both edges along the x and y directions (see Fig. 4b). This transition indicates a sole topological transition at the edge bands while the topology of the bulk bands does not change.

The topological transitions of the edge states lead to various transitions between the bulk, edge and corner states, as indicated in Fig. 4c. In a box-shaped supercell calculation, the corner

states studied in Fig. 3 merge into the bulk when θ_{in} approaches 90° due to the bulk topological transition. However, when θ_{in} approaches 25° , the corner states merge into edge states due to the edge gap closing and topological transition in the edge bands. Further decrease of the angle θ_{in} , leads to a transition from edge states to bulk states caused by the bulk topological transition at $\theta_{in} = 0^\circ$. These emergent topological transitions can be used to transfer acoustic energy between bulk, edge and corner modes. Finally, we remark that for θ_{in} close to or smaller than 25° , the edge gap is too small to support distinguishable corner states, although the Jackiw-Rebbi mechanism remains valid.

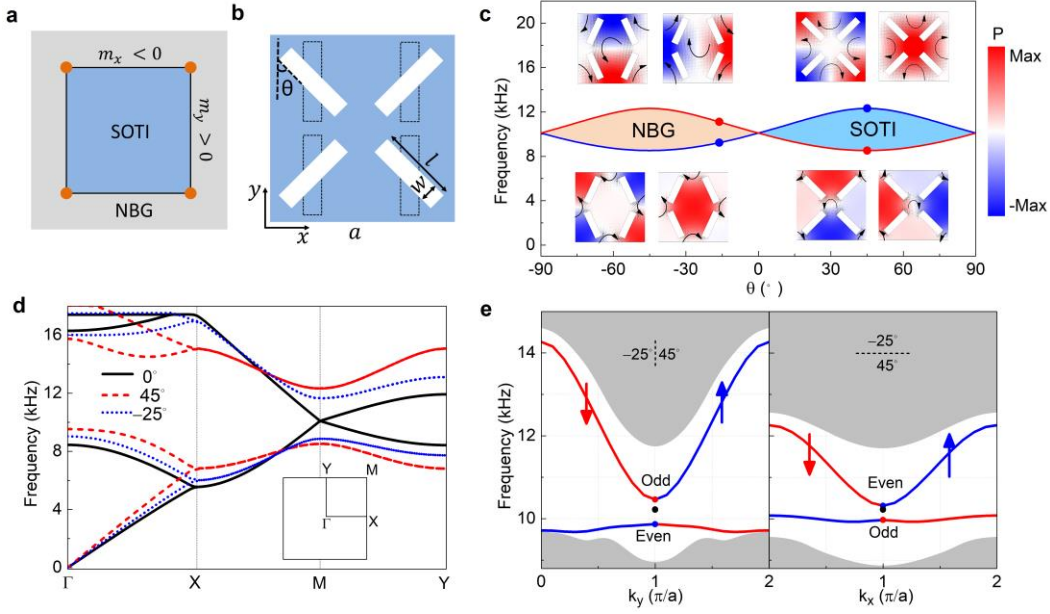


Figure 1 | Bulk, edge and corner states in SOTIs. **a**, Schematic for the corner states. The edge states on the x and y boundaries are massive Dirac waves with opposite signs of the Dirac masses, leading to topological corner states according to the Jackiw-Rebbi mechanism. **b**, The unit-cell structure of the proposed SC. **c**, The topological phase diagram of the bulk acoustic bands, with $\theta = 0^\circ, 90^\circ$ marking the transition from the NBG to the SOTI. The insets: acoustic pressure

fields of the bands above and below the gap at the M point. **d**, Band structures of the SCs with $\theta = 0^\circ$ (solid curves), 45° (dashed curves) and -25° (dotted curves), with the inset depicting the Brillouin zone. **e**, The bulk, edge and corner dispersions when the two SCs with $\theta = -25^\circ/45^\circ$ are placed together for both the y (left) and x (right) edges.

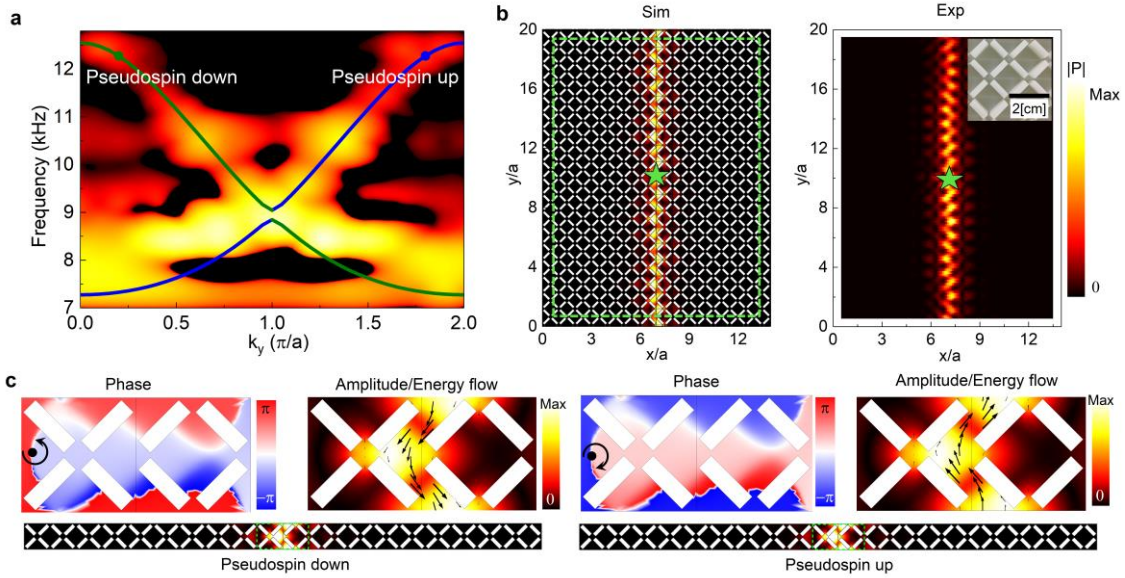


Figure 2 | Properties of the edge states. **a**, The simulated (curves) and measured (color) dispersions of the edge states. The bright color denotes the excited edge modes, of which the dispersion agrees with the simulated dispersion. **b**, Simulated (left) and measured (right) acoustic pressure fields for the edge states launched by a point source (the green star). The inset in the right panel depicts a part of the fabricated sample. **c**, The eigen pressure field distributions for the two edge states marked in **a**, with the phase and Poynting vectors (the black arrows) shown for the two unit-cells on the boundary.

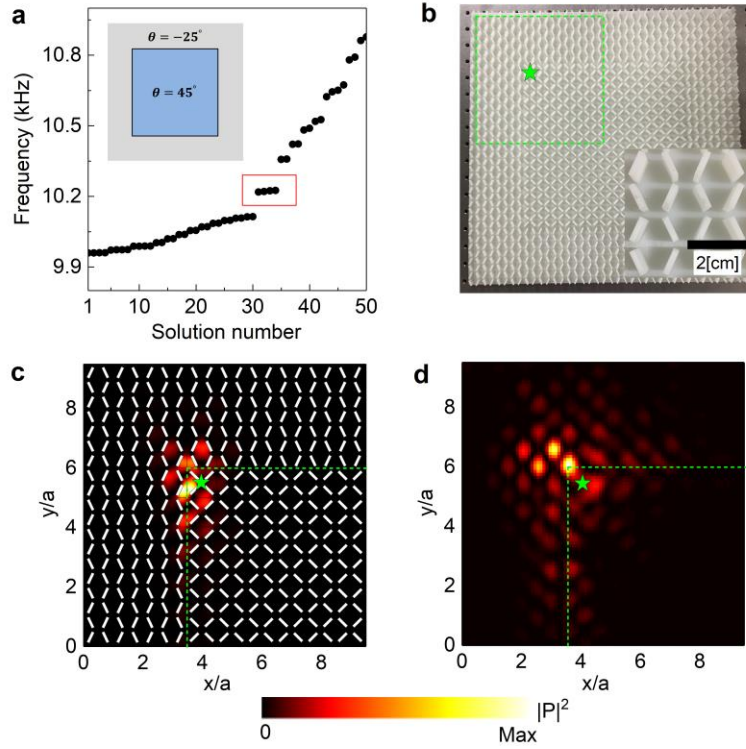


Figure 3 | Measurement of the corner states. **a**, Frequencies of the eigen-modes for a box-shaped supercell calculation (illustrated by the inset). The supercell consists of an area of $12 \times 12a^2$ SC with $\theta = 45^\circ$ enclosed by a wall of the SC with $\theta = -25^\circ$ of thickness $4a$. There are four corner states in the edge gap, denoted by the red box. **b**, Experimental set-up to detect the corner states. The distribution of the acoustic pressure field from simulation **c** and experiments **d**.

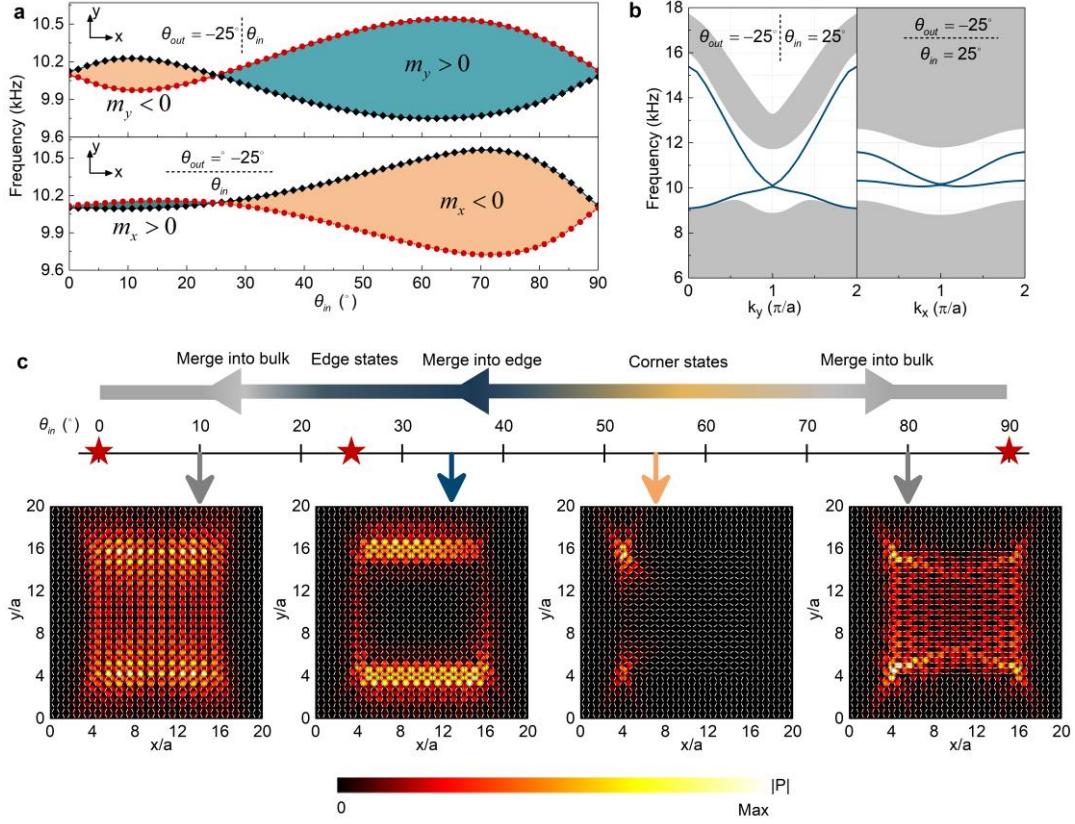


Figure 4 | Topological transitions in the edge. **a**, The edge phase diagram, which manifests the edge topological transition at $\theta_{in} = 25^\circ$, and the bulk topological transitions at $\theta_{in} = 0^\circ$ and 90° . The topologically trivial SC is chosen as $\theta_{out} = -25^\circ$. **b**, The projected band structures for the supercell with $\theta_{out}/\theta_{in} = -25^\circ/25^\circ$. The edge gap closing is observed for both edges along the y and x directions, which is a clear signature of the edge topological transition. **c**, Demonstration of various transitions among the bulk, edge and corner states, by tuning θ_{in} , which promises a topological acoustic energy exchange mechanism between bulk, edge and corner modes.

Discussion

Achieving topological transitions between the bulk, edge and corner modes in a single chip is of fundamental importance which can enable topologically protected 1D and 0D modes for integrated acoustic devices as well as topologically induced acoustic energy transfer between different dimensions. Our study uncovers the underlying physics for such hierarchical topological transitions and opens a new path for future applications of topologically protected integrated acoustic devices and topological acoustic energy/information guiding for hierarchical dimensions. Furthermore, it opens new questions important for future fundamental sciences and applications: Is it possible to extend the scenario discovered in this work to photonic or other classical wave systems? Can one realize SOTIs or third-order topological insulators for 3D sonic or photonic crystals where topological hinge states emerge? What will happen if the corner or edge states are selectively coupled to resonators with gain or loss? Will HOTIs provide design facility for advanced integrated acoustic or photonic circuits? These important questions will drive the study on HOTIs to future science and applications.

Method

Experiments

The present SC consists of bars that are made of photosensitive resin (modulus 2765 MPa, density 1.3 g/cm³). We utilize a stereo lithography apparatus to fabricate the samples: one with $w=0.15a$ and $l=0.5a$ for the edge state measurements, and, the other with $w=0.1a$ and $l=0.4a$ for the corner state measurements, where $a=2$ cm is the lattice constant. The

geometric tolerance is roughly 2 mm. The height of our samples is chosen to be 1 cm, roughly half the lattice constant. In the measurements, the samples are enclosed in the vertical direction by two flat acoustically rigid plates to form a waveguide, such that at the operating frequencies ~ 10 kHz, only 0th order mode can be excited (see Supplementary Information). This ensures that the 2D approximation is applicable. The experimental data plotted in Fig. 2(a) are collected from the following procedure. We first scan the pressure field distribution under a specific frequency excitation. The experiments are conducted using an acoustic transducer to generate acoustic sources, which are guided into the samples from channels (with diameter of ~ 4 mm) opened on the bottom flat plate of the waveguide. An acoustic detector (B&K-4939 1/4 inch microphone) is used to probe the excited pressure field from an open channel (with diameter slightly larger than the detector) on the top flat plate, and its position is controlled by an automatic stage. The data are collected and analyzed by a DAQ card (NI PCI-6251). The obtained real space data are then taken for the Fourier transform to obtain the dispersion of edge states in momentum space, where the Matlab built-in function *fft* is used. For the measurement of the edge and corner states field distributions (Figs. 2(c) and 3(d)), we use the abovementioned procedure to collect data, which are further post-processed to generate the color maps. The transmission measurements in the Supplementary Information are conducted using the same set-up, only we fix the automatic stage and sweep the input frequencies.

Simulations

Numerical simulations in this paper are all conducted using the 2D acoustic module of a commercial FEM software (COMSOL MULTIPHYSICS). The resin bars are treated as acoustically rigid boundaries. In the eigen-evaluations, all four boundaries of the unit cell are set as Floquet periodic boundaries for the data in Figs. 1(b) and 1(c). The boundaries of the

supercells are set as Floquet periodic boundaries along the edge direction, with the perpendicular direction set as plane wave radiation boundaries, for the data in Figs. 1(d), 2(a)-2(c) (left panel) and 4(a)-4(c). The boundaries of the corner samples are set as plane wave radiation boundaries, for the data in Figs. 3(a), 3(c) and 4(d)-4(f).

Acknowledgements

X.Z, Y.T, B.X and M.H.L are supported by the National Key R&D Program of China (Grant No. 2017YFA0303700), the National Natural Science Foundation of China (Grant No. 51721001) and the Academic Program Development of Jiangsu Higher Education (PAPD). H.X.W, Z.K.L and J.H.J are supported by the National Natural Science Foundation of China (Grant No. 11675116). X.Z thanks Hao Ge and Siyuan Yu for useful discussions on the experimental measurements, and Z.G. Chen for the help on simulation set-up.

Author contributions

J.H.J and M.H.L conceived the idea and guided the research. X.Z, H.X.W and Z.K.L performed the numerical simulations. H.X.W, B.X and J.H.J did theoretical analysis. X.Z and Y.T performed experimental measurements. All the authors contributed to the discussion of the results and the manuscript preparation. J.H.J, X.Z, and M.H.L wrote the manuscript.

References

[1] Thouless, D. J., Kohmoto, M., Nightingale, M. P. & den Nijs, M. Quantized Hall conductance in a two-dimensional periodic potential. *Phys. Rev. Lett.* 49, 405-408 (1982).

- [2] Haldane, F. D. M. Model for a quantum Hall effect without Landau levels: condensed-matter realization of the ‘parity anomaly’. *Phys. Rev. Lett.* 61, 2015-2018 (1988).
- [3] Hasan, M. Z. & Kane, C. L. Colloquium: topological insulators. *Rev. Mod. Phys.* **82**, 3045–3067 (2010)
- [4] Qi, X.-L. & Zhang, S.-C. Topological insulators and superconductors. *Rev. Mod. Phys.* **83**, 1057–1110 (2011).
- [5] Haldane, F. D. M. & Raghu, S. Possible realization of directional optical waveguides in photonic crystals with broken time-reversal symmetry. *Phys. Rev. Lett.* 100, 013904 (2008).
- [6] Wang, Z., Chong, Y., Joannopoulos, J. D. & Soljacic, M. Observation of unidirectional backscattering immune topological electromagnetic states. *Nature* 461, 772-775 (2009).
- [7] Hafezi, M., Demler, E. A., Lukin, M. D. & Taylor, J. M. Robust optical delay lines with topological protection. *Nat. Phys.* 7, 907-912 (2011).
- [8] Poo, Y., Wu, R., Lin, Z., Yang, Y. & Chan, C. T. Experimental realization of self-guiding unidirectional electromagnetic edge states. *Phys. Rev. Lett.* 106, 093903 (2011).
- [9] Hafezi, M., Mittal, S., Fan, J., Migdall, A. & Taylor, J. M. Imaging topological edge states in silicon photonics. *Nat. Photon.* 7, 1001-1005 (2013).
- [10] Rechtsman, M. C. et al. Photonic Floquet topological insulators. *Nature* 496, 196-200 (2013).
- [11] Khanikaev, A. B. et al. Photonic topological insulators. *Nat. Mater.* 12, 233-239 (2013).

- [12] Chen, W.-J. et al. Experimental realization of photonic topological insulator in a uniaxial metacrystal waveguide. *Nat. Commun.* 5, 6782 (2014).
- [13] Wu, L.-H. & Hu, X. Scheme for achieving a topological photonic crystal by using dielectric material. *Phys. Rev. Lett.* 114, 223901 (2015).
- [14] Xu, L., Wang, H.-X., Xu, Y.-D., Chen, H.-Y., & Jiang, J.-H. Accidental degeneracy and topological phase transitions in two-dimensional core-shell dielectric photonic crystals. *Opt. Express* 24, 18059 (2016).
- [15] Lu, L., Joannopoulos, J. D. & Soljacic, M. Topological photonics. *Nat. Photon.* 8, 821-829 (2014).
- [16] Chen, Z. G. et al. Accidental degeneracy of double Dirac cones in a phononic crystal. *Sci. Rep.* 4, 4613 (2014)
- [17] Yang, Z. J., Gao, F., Shi, X. H., Lin, X., Gao, Z., Chong, Y. D. & Zhang, B. L. Topological acoustics. *Phys. Rev. Lett.* 114, 114301 (2015)
- [18] He, C., Ni, X. Ge, H., Sun, X. C., Chen, Y. -B., Lu, M. -H., Liu, X. -P. & Chen, Y. -F. Acoustic topological insulator and robust one-way sound transport. *Nat. Phys.* 12, 1124-1129 (2016)
- [19] Jiuyang Lu, Chunyin Qiu, Liping Ye, Xiyang Fan, Manzhou Ke, Fan Zhang, Zhengyou Liu Observation of topological valley transport of sound in sonic crystals. *Nat. Phys.* 13, 369 (2017)

- [20] Xia, B. -Z. et al. Topological phononic insulator with robust pseudospin-dependent transport. *Phys. Rev. B* **96**, 094106 (2017).
- [21] Benalcazar, W. A., Bernevig, B. A. & Hughes, T. L. Quantized electric multipole insulators. *Science* **357**, 61–66 (2017).
- [22] Serra-Garcia, M. et al. Observation of a phononic quadrupole topological insulator. *Nature* **555**, 342–345 (2018)
- [23] Peterson, C. W., Benalcazar, W. A., Hughes, T. L. & Bahl, G. A quantized microwave quadrupole insulator with topological protected corner states. *Nature* **555**, 346–350 (2018).
- [24] Schindler, F. et al. Higher-order topological insulators. *Sci. Adv.* **4**, eaat0346 (2018)
- [25] Langbehn, J., Peng, Y., Trifunovic, L., Oppen, F. V. & Brouwer, P. W. Reflection-symmetric second-order topological insulators and superconductors. *Phys. Rev. Lett.* **119**, 246401 (2017)
- [26] Song, Z. D., Fng, Z. & Fang, C. (d-2)-dimensional edge states of rotation symmetry protected topological states. *Phys. Rev. Lett.* **119**, 246402 (2017)
- [27] Kunst, F. K., Miert, G. V., & Bergholtz, E. J. Lattice models with exactly solvable topological hinge and corner states. *Phys. Rev. B* **97**, 241405(R) (2017)
- [28] Ezawa, M. Higher-order topological insulators and semimetals on the breathing kagome and pyrochlore lattices. *Phys. Rev. Lett.* **120**, 026801 (2018)

[29] Xie, B. Y., Wang, H. F., Wang, H. -X., Zhu, X. Y., Jiang, J. -H., Lu, M. H. & Chen, Y. F. Second-order photonic topological insulator with corner states. Preprint at <https://arxiv.org/abs/1805.07555v2> (2018).

[30] Lidorikis, E., Sigalas, M. M., Economou, E. N. & Soukoulis, C. M. *Phys. Rev. Lett.* **81**, 1405 (1998).

[31] Jackiw, R. & Rebbi, C. Solitons with fermion number $1/2$. *Phys. Rev. D* **13**, 3398-3409 (1976).

[32] It is also checked that by deforming the meta-atom configurations in each unit-cell in a way that ensures that each primitive cell has four meta-atoms and keeps the mirror symmetry, the underlying physics is identical to what we present in this article (see Supplemental Information).

[33] Bernevig, B. A., Hughes, T. L., & Zhang, S.-C.. Quantum Spin Hall Effect and Topological Phase Transition in HgTe Quantum Wells. *Science* **314**, 1757-1761 (2016).

[34] Noh, J. et al. Topological protection of photonic mid-gap defect modes. Preprint at <https://arxiv.org/abs/1611.02373>

[35] Li, F.-F. et al. Topological light-trapping on a dislocation. *Nat. Commun.* **9**, 2462 (2018).